10

BURIED, 2-D PENETRABLE OBJECTS ILLUMINATED BY LINE SOURCES: FFT-BASED ITERATIVE COMPUTATIONS OF THE ANOMALOUS FIELD

D. Lesselier and B. Duchêne

10.1 Introduction

We discuss the frequency-domain scattering of cylindrical compressional (P) waves by a cylindrical target (with axis parallel to z) buried in the lower of two half-spaces separated by a horizontal planar interface (the $y - z$ plane). All media are linear, isotropic, non viscous fluids and variations of density are neglected. We consider targets whose transverse dimensions (in the $x - y$ plane) are of the order of the wavelength λ_2 in the lower medium or larger, and whose sound velocity and attenuation may vary arbitrarily with position (x, y). The field sources consist of a finite number of time-harmonic line sources parallel to the axis of the target and placed on a horizontal line above the interface. For each source we are interested in the anomalous field

(the difference between the total field and the field that exists in the absence of the target) observed above the interface along the same line or another one (still horizontal). Indeed, variations of anomalous field are directly linked with the acoustical or geometrical parameters of the target and can be used to probe such parameters if unknown, i.e., to solve an inverse scattering problem. In our case, we use diffraction tomography algorithms to image the target using linear arrays of sources and receivers usually $\lambda_2/2$-stepped, e.g., [1–2]. Obvious applications of imaging procedures of buried structures in a plane-layered medium (ours or any others which might be devised in this situation) can be found in civil and biomedical engineering [3–5]. In a first step, many simulations of these imaging procedures are needed. Therefore, we must have a fast and accurate computational procedure to generate the synthetic data (i.e., the anomalous field along the probing line for various targets, embedding media and illuminations) in taking into account all scattering phenomena occuring in the entire structure (the target and its environment). Indeed, most imaging techniques are linearized solutions of the inverse scattering problem based on first-order field approximations (e.g., Born's or Rytov's), but they must be able to work with data that are not calculated using hypotheses of weak scattering [6].

So far, we have developed an effective numerical solution of a similar though less involved scattering problem: the cylindrical target is located in a homogeneous medium and the field sources are located at infinity and generate plane-waves [7]. To do so, we start from the second kind Fredholm integral equation satisfied by the field (or the induced sources) in the target which we easily obtain by applying Green's theorem. Then, a method of moments with pulse-basis and Dirac delta weight-function, e.g., [8–9], yields a discrete version of this equation whose solution is calculated (i) : either directly with a Gauss-Jordan inversion algorithm, or (ii) : using conjugate-gradient algorithms (that minimize the residual or the error on the solution itself), or (iii) : by expansion of the pressure into Neumann's series (with active extrapolation to speed up the convergence). The convolution products which appear in each iteration are computed by 2-D Fast Fourier Transforms. But, when the target is embedded in a stratified space, the kernel of the integral equation is much more complicated; the free-space Green's function is replaced by the Green's function of the stratified space which takes into account transmission through and reflection upon ev-

ery interface and which is now only known in closed form in the spectral domain (it is given by means of Fourier integrals). Convolution and correlation products with respect to depth have to be simultaneously calculated. Nevertheless, direct solutions (first) and iterative ones (next) have been developed for planar illuminations [1], [10], and (recently) for line-sources [2]. Their performances are fair but they do not employ FFT algorithms to compute the convolution and correlation products and consequently require high CPU time, particularly for large and/or high-contrast targets; when we deal with a large number of illuminations, as is frequent in imaging problems, this may become prohibitive.

The purpose of this chapter is then to show how we can obtain fast iterative solutions of a typical scalar scattering problem in fluid acoustics (the buried target). The numerical simulations are performed in ultrasonics. However, the same approach would be valid fully in electromagnetics for lossy dielectric cylindrical inhomogeneities immersed in a plane-layered medium when the electric field is polarized along their axes, even though the strong influence of absorption and the fact that the half-space where the sources are located would generally be the one with lower index might lead to somewhat different conclusions from a computational point-of-view.

To our knowledge, a similar solution of this (these) problem(s) has not yet been presented in the literature. Obviously, there exist very interesting numerical investigations of exact solutions of the direct scattering problem by buried targets. We may quote [11], where computational efficiency is attained by using a Galerkin method of moments with plane-wave basis and specializing the procedure to a homogeneous penetrable rectangular cylinder (illuminated by a time-harmonic line-source). T-matrix style solutions in both electromagnetics and acoustics have also been developed for targets that are either homogeneous or could be divided into several homogeneous regions, with some symmetry (for example a stratified cylinder), but numerical studies seem to have been limited to perfectly hard or soft homogeneous targets [12–13 (see in addition refs. quoted)]. Boundary-integral formulations are also employed when dealing with such scatterers (where integrals along the contours of the subregions, but also along the interface, or all interfaces in case of a multilayered embedding, are considered), the calculations being mostly carried out directly in time-domain, e.g., [14–15]. Also, an involved but powerful method of computation of the seismograms due

to a (rigid) underground scatterer and which takes part of its inspiration from that observation is investigated in [16]. Finally, one could apply Finite-Elements techniques, which are commonly used in seismic modeling of lateral inhomogeneities (in an otherwise plane-layered earth) or in studies about magnetic non-destructive testing of defaults in metal structures, and whose pros and cons (in particular due to artificial side reflections) are well-documented, but which we will not dwell upon herein.

Two of the main numerical techniques we apply in our investigation are a simple version of the method of moments, and iterative solutions of the resulting set of discrete equations. The method of moments has been widely used these last twenty years or so, and everybody is now aware of its very many applications. Some of them in electromagnetics have been reviewed recently [17]. A concise and up-to-date exposition of the method itself illustrated by some examples can be found in [8], and we may also refer the reader to a broad and thoughtful survey of so-called computational electromagnetics [9]. As for the topic of iterative solutions of radiation and scattering problems, a great number of papers have been published since the original study on conjugate-gradient [18], and some controversy also went on in the mid-80's (as is summarized, e.g., in [19]). Here, we will leave aside the abundant literature on iterative solution of the inverse scattering problem (for example, a thorough investigation of optimal solutions in 1-D cases and many references could be found in [20], and various other examples of optimal research are given in [21]) and in short we would only like to point-out, without pretending to exhaustivity, some useful references:

(i) : an early and quite complete article (published in 1967) on iterative solutions of operator equations [22];

(ii) : an investigation [23] of scattering by perfectly conducting cylinders published in 1973, which (in particular) uses a method of moments solution with a conjugate-gradient algorithm for one of the first times in computational electromagnetics.

(iii) : three papers published in the early 80's, where it was shown how large linear systems of equations like those obtained when using methods of moments can be solved in an effective manner [24], or how functional minimizations of integrated-square errors can be devised in a very general setting and still yield practical numerical solutions of real-world scattering problems ([25] in 2-D transient linear acoustics and [26] in microwave hyperthermia);

(iv) : several of the papers published at the beginning of 1986 in a (delayed) special issue of *Electromagnetics* on Iterative Methods in Electromagnetics [27–30], [7] (the other papers of the issue mainly dealt with periodic structures, a subject of great interest but a bit out of the scope of our chapter); many different aspects of iterative solutions and various applications are investigated herein, with, in particular, discussion of "new" tools, i.e., FFT's (see also [31], which motivated the authors to use them successfully, and [32]) and a lot of references are obviously made available.

(v) : recent contributions (see also [19] which we already refered to) that either give a comprehensive survey of conjugate-gradient-like algorithms including handy computer programs [33] or detail the performances of one of them (generalized biconjugate) [34], or investigate both theoretically and numerically the relationship between eigenvalues of a continuous operator and of its discrete counterpart as produced by a method of moments (and, consequently, how the convergence rate of a conjugate-gradient algorithm varies) [35–36], or deal with the key problem of preconditioning [37];

(vi) : a detailed analysis of FFT-conjugate-gradient techniques applied to calculation of scattering by a dielectric cylinder illuminated under oblique incidence [38]. (Note that the case of the dielectric cylinder under TE and TM illumination, which has been the subject of well-known early applications of the method of moments with direct inversion of the matrix system [39–40], is one of the test-cases studied in [35], whereas FFT-iterative techniques are systematically used in our laboratory since 1985 to calculate scattering by cylinders with arbitrary shapes in fluid acoustics, as is briefly described in [7], or in microwaves, e.g., [41].)

The solution we propose is based on the method of moments (pulse basis + delta functions) and uses either (i) : a conjugate-gradient algorithm that minimizes residuals, or (ii) : a conjugate-gradient algorithm that minimizes solution errors, or (iii) : Neumann's series expansion with Aitken's extrapolation (one of the simplest extrapolation algorithms, see in particular [42]) when convergent (it would be computationally prohibitive to establish *a priori* the convergence of this expansion but it is easily appraised after one or at the most a few iterations). 2-D FFT algorithms are employed to compute all convolution and correlation products [43], while 1-D FFT algorithms enable us to calculate the Fourier integrals as is usual. In particular, we show how

the various procedures (conjugate-gradients, Neumann's series) behave with respect to each other, and as a function of the parameters of the line source and of the target. (These parameters are also of prime importance when we look at the perfomances of any imaging technique for concealed targets.) As we would like to be able to consider a large number of sources, the importance of a good compromise between number of operations and size of the storage, both parameters being directly related to the accuracy of the computed field, is emphasized.

10.2 Theory

10.2.1 The integral formulation

Let us refer to Fig. 10.1. We consider two homogeneous fluid half-spaces D_1 and D_2 with respective sound velocites c_1 and c_2 and attenuations α_1 (henceforth reduced to zero) and α_2 which are separated by a horizontal planar interface located at $x = 0$. The fluid cylindrical target, of limited cross-section with arbitrary shape D_Ω in the x-y plane and with sound velocity c_Ω and attenuation α_Ω varying with position (x, y), is embedded in the lower half-space and is illuminated, at the operating frequency f ($f = \omega/2\pi$), by a line source or a set of line sources located in the upper half-space. The density is constant throughout space and a time dependence $e^{-j\omega t}$ is assumed. In the following, we restrict ourselves to velocity c_2 larger than c_1, with the implicit assumption that the upper space consists of water, but this is not an obligation. In that particular case, if we would like to go back to electromagnetics, we easily see that we would be dealing with propagation of E-polarized cylindrical waves from a lossless medium (D_1) with dielectric index $n_1 = 1$ to a (possibly lossy) medium (D_2) with lower index (its real part will be $n_2 = c_1/c_2 < 1$) where some inhomogeneous cylinder with arbitary index is located.

Let us now describe the integral representation of the fields, partly for the sake of completeness since the parallel case of a planar illumination is already treated [10] and partly because it is easier to explain the numerical procedure once this representation is established.

As is well-known, the scalar pressure field $p(x, y)$ observed at any point (x, y) when the target is illuminated by a line-source located at (x_S, y_S) in half-space D_1 satisfies, in the distribution sense, the wave

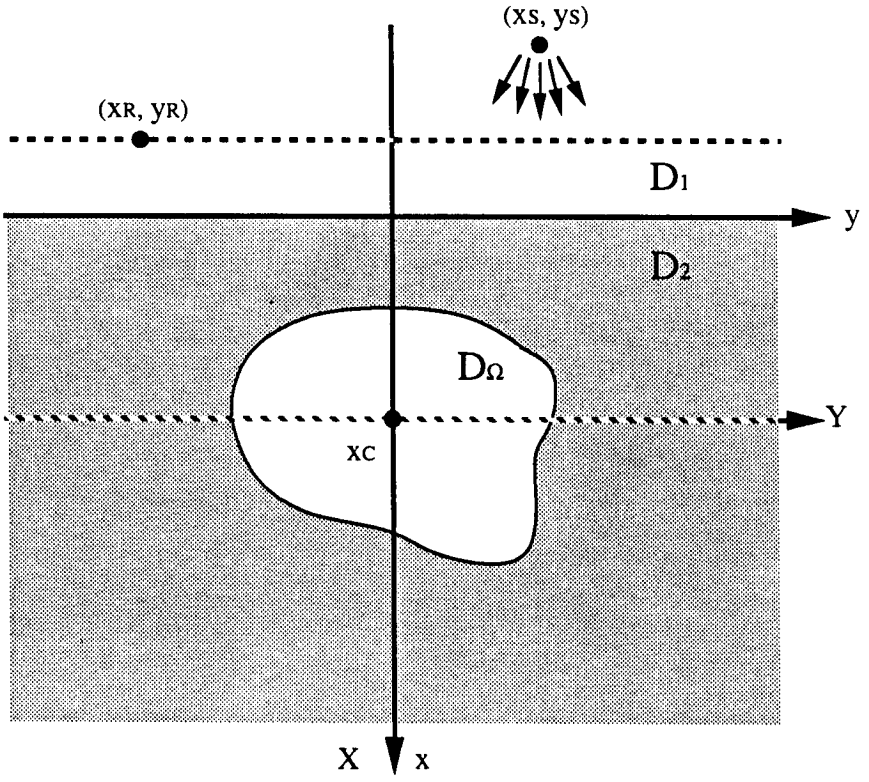

Figure 10.1 Geometry of the scattering problem.

equation:

$$\Delta p(x,y) + k^2 p(x,y) = -\delta(x - x_S, y - y_S)\delta_{m1}$$

$$(x,y) \in D_m;\ k \equiv k_m;\ m = 1,2,\Omega \tag{10.1}$$

where k_m is the complex-valued propagation constant of medium $m(k_m = \omega/c_m + j\alpha_m$, with k_Ω function of space),δ is the Dirac distri-

bution and δ_{m1} is the Kronecker symbol. Boundary conditions (continuity of the pressure and of its normal derivative) are implied, and the pressure satisfies a Sommerfeld radiation condition at infinity.

Pressure p is obtained by applying Green's theorem to functions p and G_{mn}, with p satisfying (10.1) and G_{mn} being the Green's function of the layered medium (i.e., without the scatterer). This function satisfies in the distribution sense:

$$\Delta G_{mn}(x,y,x',y') + k_m^2 G_{mn}(x,y,x',y') = -\delta(x-x',y-y')\delta_{mn}$$

$$(x,y) \in D_m;\ (x',y') \in D_n;\ m=1,2;\ n=1,2 \qquad (10.2)$$

and the same boundary and radiation conditions as those of p hold. Note that $G_{mn}(x,y,x',y')$ represents the field observed at (x,y) when a line source is located at (x',y'), the target being absent. G_{mn} is known in closed form in the spectral domain, after expansion into plane waves:

$$G_{mn}(x,y,x',y') = \frac{1}{2\pi}\int_{-\infty}^{+\infty} g_{mn}(x,\alpha,x',y')e^{j\alpha y}d\alpha \qquad (10.3)$$

and its expression depends upon the respective position of the line source (x',y') and of the observation point (x,y). We define the usual propagation factors β_1 and β_2 as follows:

$$\beta_m = \sqrt{k_m^2-\alpha^2},\ \ \mathrm{Im}\,\beta_m \geq 0, m=1,2 \qquad (10.4)$$

When source and observation points are on the same side m with respect to the interface: (x',y') and $(x,y) \in D_m (m = 1 \text{ or } 2)$, G_{mm} comprises both a singular term (superscript s) and a regular term (superscript ns) with

$$g_{mm}(x,\alpha,x',y') = g_{mm}^{ns}(x,\alpha,x',y') + g_{mm}^{s}(x,\alpha,x',y')$$

$$g_{mm}^{ns}(x,\alpha,x',y') = j(-1)^m \frac{1}{2\beta_m}\frac{(\beta_2-\beta_1)}{(\beta_1+\beta_2)}e^{j\beta_m(|x|+|x'|)}e^{-j\alpha y'}$$

$$g_{mm}^{s}(x,\alpha,x',y') = j\frac{1}{2\beta_m}e^{j\beta_m|x-x'|}e^{-j\alpha y'} \qquad (10.5a)$$

When source and observation points are on opposite sides: $(x', y') \in D_n$, $(x, y) \in D_m$ ($m = 1$, $n = 2$, and conversely), we only have regular terms (denoted with superscript ns), which correspond to

$$g_{mn}(x, \alpha, x', y') = g^{ns}_{mn}(x, \alpha, x', y') = j \frac{e^{j(\beta_n |x'| + \beta_m |x|)}}{(\beta_1 + \beta_2)} e^{-j\alpha y'} \quad (10.5b)$$

The singular term in (10.5a) is nothing other than the Fourier transform of the 2-D Green's function in free-space (with propagation constant k_m):

$$\begin{aligned} G^s_{mm}(x, y, x', y') &= \frac{j}{4} H^1_0(k_m \sqrt{(x - x')^2 + (y - y')^2}) \\ &= \frac{1}{2\pi} \int_{-\infty}^{+\infty} g^s_{mm}(x, \alpha, x', y') e^{j\alpha y} d\alpha \end{aligned} \quad (10.6)$$

with H^1_0 the first-kind zero-order Hankel function.

We observe that $G_{mn}, m \neq n$, is a function of three variables: x, x' and difference $(y - y')$, that G_{mm} is a function of two variables: either the differences $(x - x')$ and $(y - y')$ for the singular part, or the sum $(x + x')$ and the difference $(y - y')$ for the regular part (with x and x' of the same sign). Then, we may substitute $G_{mn}(x, x', y - y')$ to $G_{mn}(x, x', y, y')$, $G^s_{mm}(x - x', y - y')$ to $G^s_{mm}(x, x', y, y')$ and $G^{ns}_{mm}(x + x', y - y')$ to $G^{ns}_{mm}(x, x', y, y')$.

We introduce the contrast function χ that is characteristic of the target D_Ω with respect to its embedding in D_2, and the induced sources J_Ω within this target:

$$\begin{aligned} \chi_\Omega(x, y) &= k^2_\Omega(x, y) - k^2_2 \\ J_\Omega(x, y) &= \chi_\Omega(x, y) p(x, y) \end{aligned} \quad (10.7)$$

Applying Green's theorem to functions p and G_{mn} over a domain which covers the entire space $\mathbf{R}^2$, and using the fact that the target is totally contained in the lower half-space $D_2 (D_2 \supset D_\Omega)$, we easily get the volume integral formulation of the induced sources

$$\begin{aligned} J_\Omega(x, y) =& J_0(x, y) + \chi_\Omega(x, y) \times \\ & \iint_{D_\Omega} J_\Omega(x', y') \left[G^{ns}_{22}(x + x', y - y') + G^s_{22}(x - x', y - y') \right] \\ & dx' dy' \end{aligned} \quad (10.8a)$$

with a source term $J_0(x,y)$ proportional to the incident field (the field that exists in the absence of the target)

$$J_0(x,y) = \chi_\Omega(x,y) G_{21}(x, x_S, y - y_S) \tag{10.8b}$$

Let us now consider that we place a set of receivers at different points (x_R, y_R) along a probing line parallel to the interface and located in the upper half-space ($(x_R, y_R) \in D_1$). The anomalous field p_A on this probing line for a given location of the source (x_S, y_S) is obtained by straightforward integration over D_Ω:

$$p_A(x_R, y_R) = \iint_{D_\Omega} J_\Omega(x', y') G_{12}(x_R, x', y_R - y') dx' dy' \tag{10.9}$$

10.2.2 The discrete formulation

Solution of the problem summarized by (10.8) and (10.9) is carried out by the means of a method of moments with pulse-basis functions and point-matching. First, we assume that the target cross-section D_Ω is inscribed into a square centered at $x = x_C$, $y = y_C$ (y_C is equated to 0 for the sake of computational simplicity) and we define new coordinates $X = x - x_C$ and $Y = y - y_C$, which we henceforth use systematically. Then, we divide this square into a number N^2 (N *odd* number) of square cells with side Δ small with respect to the local wavelength. We then have N cells along each axis of coordinates centered at

$$(X_p, Y_q) = (p\Delta, q\Delta);$$

$$p, q = -(N-1)/2, \ldots, -1, 0, 1, \ldots, +(N-1)/2; \tag{10.10}$$

$$X_p \geq -x_C$$

In each cell (p,q) we assume that contrast and field remain constant with respective values $\chi(X_p, Y_q)$ and $p(X_p, Y_q)$, which yield constant sources $J_\Omega(X_p, Y_q)$. Let us point out that the size Δ of the cell, equated to a fraction of the wavelength in D_2, is independent of N (N characterizes the overall size of the target).

The induced source at center (X_m, Y_n) of a given cell (m,n) is expressed as a linear function of the induced sources in the N^2 cells of

the mesh, this particular cell included, i.e., at the N^2 points (X_p, Y_q). First, we write at any (X_m, Y_n)

$$\iint_{D_\Omega} J_\Omega(X', Y') G_{22}(X_m, Y_n, X', Y') dX' dY'$$

$$= \sum_{p,q} J_\Omega(X_p, Y_q) \iint_{\text{cell}(p,q)} G_{22}(X_m, Y_n, X', Y') dX' dY'$$

$$= \sum_{p,q} J_\Omega(X_p, Y_q) H_{22}(X_m, Y_n, X_p, Y_q) \tag{10.11a}$$

where reversing order of integration with respect to α and with respect to Ω yields

$$H_{22}(X_m, Y_n, X_p, Y_q) = \frac{1}{2\pi} \int_{-\infty}^{+\infty} \tag{10.11b}$$

$$\left[\iint_{\text{cell}(p,q)} g_{22}(X_m, \alpha, X', Y') dX' dY' \right] e^{j\alpha Y_n} d\alpha$$

subject to careful self-patch integration (when cells (p, q) and (m, n) coincide). In order to get simpler expressions, we take into account the dependence of the regular part and of the singular part of the Green's function G_{22} upon $(X + X')$ and $(X - X')$ respectively, and upon $(Y - Y')$ for both. The finite-valued, integrated terms H_{22} are obtained after a few calculations.

(i): $H_{22}^{ns}(X_m + X_p, Y_n - Y_q)$ results from analytically carrying out the integration of the non-singular term $(2\pi)^{-1} g_{22}^{ns}(X_m, \alpha, X', Y') e^{j\alpha Y_n}$ versus X' and Y' on each square cell centered at (X_p, Y_q) and is given by a Fourier integral

$$H_{22}^{ns}(U, V) = \int_{-\infty}^{+\infty} C(\alpha) e^{j\beta_2 U} e^{2j\beta_2 x_C} e^{j\alpha V} d\alpha$$

$$C(\alpha) = B(\alpha) \frac{\beta_2 - \beta_1}{(\beta_2)^2} \tag{10.12a}$$

$$B(\alpha) = j \frac{\sin(\alpha\Delta/2)}{\pi\alpha} \frac{\sin(\beta_2\Delta/2)}{\beta_2 + \beta_1}$$

$U(= X_m + X_p)$ is always larger than or equal to $-2x_C$ in the above integrand. Note also that there is a factor equivalent to β_2 in the denominator when α is close to k_2. The Fourier integral is absolutely convergent provided that $U \geq -2x_C$ and will be computed by means of FFT algorithms without particular problems (with adequate sampling at values of α other than k_2) as is said in subsection 10.2.3.

(ii): $H^s_{22}(X_m - X_p, Y_n - Y_q)$ results from analytically carrying out the integration of the free-space Green's function (we take into account relation (10.6)) after replacing as is usual the square cell by a circular disk of the same area (radius $d = \Delta/\sqrt{\pi}$); it only depends upon the distance $R = \sqrt{(X_m - X_p)^2 + (Y_n - Y_q)^2}$ between integration point (X_p, Y_q) and observation point (X_m, Y_n) and is known in closed form

$$H^s_{22}(R) = \begin{cases} k_2^{-2}[0.5j\pi k_2 d H_1^1(k_2 d) - 1] & \text{if } (m,n) = (p,q) \\ 0.5j\pi d k_2^{-1} H_0^1(k_2 R) J_1(k_2 d) & \text{if } (m,n) \neq (p,q) \end{cases} \tag{10.12b}$$

with H_1^1 the first-kind first-order Hankel function and J_1 the first-order Bessel function.

Now, we are able to write down a system of N^2 linear equations, one for each cell (X_m, Y_n):

$$J_\Omega(X_m, Y_n) - \chi_\Omega(X_m, Y_n)\left\{\sum_{p,q} J_\Omega(X_p, Y_q)\left[H^{ns}_{22}(X_m + X_p, Y_n - Y_q) + H^s_{22}(X_m - X_p, Y_n - Y_q)\right]\right\} = J_0(X_m, Y_n) \tag{10.13}$$

where the source term $J_0(X_m, Y_n)$ is deduced from (10.5b)(10.8b) after simply changing the set of coordinates and is given by

$$J_0(X_m, Y_n) = \chi_\Omega(X_m, Y_n) G_{21}(X_m, X_S, Y_n - Y_S)$$

$$G_{21}(X_m, X_s, U) = \frac{j}{2\pi}\int_{-\infty}^{+\infty} (\beta_1 + \beta_2)^{-1} e^{-j\beta_1 X_S} e^{j\beta_2 X_m} e^{-j(\beta_1 - \beta_2)x_C} e^{j\alpha U} d\alpha \tag{10.14}$$

with $X_S = x_S - x_C$ and with $Y_S = y_S$ equated to $\pm s\Delta$, s positive integer (this Fourier integral will be calculated like H_{22} by means of a FFT algorithm).

Once the induced sources are computed, in one way or another, the anomalous field observed above the interface at (X_R, Y_R), then at height $|X_R + x_C|$, with Y_R also taken as a multiple of $\Delta(Y_R = \pm r\Delta)$, is

$$p_A(X_R, Y_R) = \sum_{m,n} J_\Omega(X_m, Y_n) H_{12}(X_R, X_m, Y_R - Y_n) \qquad (10.15a)$$

integration on the square cell centered at (X_m, Y_n) yielding H_{12}

$$H_{12}(X_R, X_m, V) = \int_{-\infty}^{+\infty} B(\alpha) \frac{2}{\beta_1} e^{-j\beta_1 X_R} e^{j\beta_2 X_m} e^{-j(\beta_1 - \beta_2)x_C} e^{j\alpha V} d\alpha \qquad (10.15b)$$

where B is defined in (10.12a) above.

Several direct (Gauss-Jordan,...) and iterative (conjugate-gradient, ...) techniques can be applied in order to calculate the solution of the linear system $AJ = J_0$ with rank N^2 which we easily deduce from (10.13). Also

(i) : the unknown sources could be expanded into Neumann's series (which is like solving the system $J = A'J + J_0$ where $A' = I - A$, I identity matrix, by means of a fixed-point algorithm) and very fast convergence observed in the case of low-contrast structures that are frequently encountered in fluid ultrasonics when, in addition, active extrapolation is employed,

(ii) : we could simply be content with Born's approximated anomalous field (equating J_Ω to J_0 in (10.9)).

When equations are of the convolutional form and iterative solution methods are applied, it is well-known that using Fast Fourier Transform algorithms to estimate the discrete convolution products at each iteration will speed up the procedure, without loss of accuracy if this is done carefully enough (in particular to avoid aliasing [31]).

However, in the case of a buried scatterer as herein, using such FFT algorithms does not appear so easy at first sight because of the complexity of the kernel of the integral equation (10.8a) or of its discrete counterpart (10.13), since both convolution products (which arise with the singular part of the Green's function) and correlation products (which arise with the regular part) with respect to depth must be calculated, in addition to convolution products with respect to the horizontal coordinate (in both cases).

We can still employ a "brute force" procedure in order to calculate and sum up all the discrete terms involved in the expressions of the

coefficients of the matrix A and of the anomalous field, as we did in [1] in the case of a plane illumination and in [2] with line sources. Therefore, in addition to computations of H_{22}^s for $N(N+1)/2$ different values of the argument R in (10.12b), we have to compute at least

(i) : N one-dimensional FFT's with respect to α in order to obtain the values of G_{21} at each point $X_m = \pm m\Delta, m = 0, 1, \ldots, (N-1)/2$ and for any $Y_n - Y_S = (n-s)\Delta$ needed (see (10.14)). Such FFT's are performed using a large number of $\alpha_i = \pm i\Delta\alpha, i = 0, 1, \ldots, N_\alpha$, with step $\Delta\alpha = 2\pi/\Delta$; for example, $2N_\alpha = 2048$. (This number must be larger than $\mathrm{Sup}(2|n-s|)$.)

(ii) : $2N-1$ one-dimensional FFT's with respect to α in order to obtain the values of H_{22}^{ns} for each value taken by $X_m + X_p = \pm i\Delta, i = 1, 2, \ldots, N$ and for any $Y_n - Y_S$ needed (see (10.12a) and observations made above in (i)). .

(iii) : N one-dimensional FFT's with respect to α are also required to compute H_{12} at each X_m in D_Ω and at any $Y_n - Y_R$ needed (see (10.15b)) which is exactly the kind of computation we effected to get G_{21} (put Y_S instead of Y_R in (i)).

Obviously, the main task remains, that is calculate the solution of the $N^2 * N^2$ matrix system $AJ = J_0$. We can do it directly : at least $(N^2)^3/3$ operations are required, or we can do it iteratively : at least N^4 operations per iteration for Neumann's series expansion or $2N^4$ for a conjugate-gradient algorithm are required, the total number of iterations being at most equal to the rank N^2 (we hope to get accurate results — and generally do — with much less).

Even though we can obtain fair results in so doing, the computational burden of the above approach may become excessive. (It would be straightforward to compute the summations that involve the singular part of the Green's function G_{22} by means of FFT algorithms, and it will avoid some operations, but the contributions of the regular part are still to be accounted for.) This is especially true

(i) : when we have to deal with targets D_Ω that are of high-contrast with respect to D_2 or/and are embedded in a medium D_2 very different from D_1 (we generally observe that a large number of iterations are required to obtain good results),

(ii) : when the target is large with respect to the wavelength in D_2 (even though the convergence of the iterative procedure often remains quite good, manipulating large complex-valued matrices is time-consuming and may even need too large a share of the computer re-

sources),

(iii) : when the number of illuminations is high as we have to repeat the iterative procedure all over for each incident field, even though taking the induced sources computed for a given illumination as initial values to compute those associated to the next one may spare us some iterations when the characteristics of the two illuminations are not too different (indeed, we are closer to the exact solution, but, at least in the scalar scattering cases we considered until now, it did not change the overall performances of the iterative procedure much).

Consequently, we have devised a set of iterative procedures that fully take into account the particular dependence upon spatial variables X and Y, i.e., which use FFT algorithms to compute both convolution and correlation products, as is described in the next subsection.

10.2.3 FFT implementation of the iterative solutions

First, let us denote $\otimes_X$ or $\otimes_Y$, the convolution products with respect to X or Y, and $©_X$ the correlation ones with respect to X (after changing coordinates). Now, let us limit ourselves to products with respect to X, since the convolution products with respect to Y could be dealt with in the same fashion as the convolution ones with respect to X. Then, introducing for the sake of the exposé two complex-valued functions of a real variable: $X \in \mathbb{R} \rightarrow E(X)$ and $F(X) \in \mathbf{C}$, with E null outside $[-(N-1)\Delta/2, +(N-1)\Delta/2]$ and F defined on the entire line $]-\infty, +\infty[$, we are able to write identities like:

$$\begin{aligned} e(X) &= \int_{-(N-1)\Delta/2}^{+(N-1)\Delta/2} E(X')F(X-X')dX' \\ &= \int_{-\infty}^{+\infty} E(X')F(X-X')dX' \equiv E \otimes_X F \\ f(X) &= \int_{-(N-1)\Delta/2}^{+(N-1)\Delta/2} E(X')F(X+X')dX' \\ &= \int_{-\infty}^{+\infty} E(X')F(X+X')dX' \equiv E©_X F \end{aligned} \qquad (10.16a)$$

Straightforward application of Fourier transforms then yields

$$e(X) = FT^{-1}\left[FT(E) \times FT(F)\right]$$

$$f(X) = FT^{-1}\left[\overline{(FT(\bar{E}))} \times FT(F)\right] \qquad (10.16b)$$

where FT and FT^{-1} denote application of a direct and of an inverse Fourier Transform on the function of interest (which should be defined on the entire line $]-\infty, +\infty[$), with usual overbar mark chosen for conjugate.

Since we deal with finite discrete summations after applying the method of moments, i.e., since we have to calculate terms like:

$$e(X_m) = \sum_{p=-(N-1)/2}^{+(N-1)/2} E(X_p)F(X_m - X_p)$$

$$f(X_m) = \sum_{p=-(N-1)/2}^{+(N-1)/2} E(X_p)F(X_m + X_p) \qquad (10.17a)$$

$$m = \pm i, i = 0, 1, \ldots, (N-1)/2$$

we can do it with similar accuracy and at considerable saving over direct operations by means of one-dimensional Fast Fourier Transforms algorithms:

$$\mathbf{e} = FFT^{-1}\left[FFT(\mathbf{E}) \times FFT(\mathbf{F})\right]$$

$$\mathbf{f} = FFT^{-1}\left[\overline{(FFT(\bar{\mathbf{E}}))} \times FFT(\mathbf{F})\right] \qquad (10.17b)$$

where FFT and FFT^{-1} mark that we respectively take the direct and inverse Fast Fourier Transform of a discrete sequence (a row vector typed in bold style). Each sequence (**e**, **f**, **E** and **F**) in the above relations consists of M elements (M *even* number) at $X_m = \pm m\Delta, m = 0, 1, \ldots, M/2$ ($-M\Delta$ is excluded). We emphasize the following.

(i) : M must be larger than (or at least equal to) twice the number N of elements in the discrete summations ($M \geq 2N$) in order to avoid aliasing, and M is usually equated to the closest integer power of 2 for taking advantage of the most efficient FFT algorithms (in the following, M is always larger than $2N$).

(ii) : Extension of E to M elements is done ("zero-padding") by setting $\mathbf{E}(X_m = m\Delta) = 0$ for $m = +(N-1)/2 + 1, \ldots, M/2$ and for

$m = -(N-1)/2-1,\ldots,-M/2+1$, and by keeping the same N central samples.

(iii) : $\mathbf{F}$ is made of M elements by setting $\mathbf{F}(X_m = m\Delta) = 0$ for $m = N,\ldots,M/2$ and for $m = -N,\ldots,-M/2+1$, and by keeping the same $2N-1$ central samples, as we are only interested in the N central elements of $\mathbf{e}$ and $\mathbf{f}$.

(iv) : $\mathbf{e}$ and $\mathbf{f}$ consist of M samples, whose N central ones are the elements of e and f given in (10.17a); these elements are calculated exactly. (Note that $\mathbf{e}$ and $\mathbf{f}$ will always be multiplied by an array which represents the contrast function χ_Ω and whose only the N central values are non zero.)

Using the preceding observations, we are now able to efficiently solve our 2-D scattering problem. The induced sources formulation becomes (with condensed notations)

$$J_\Omega = J_0 + \chi_\Omega[J_\Omega \copyright_X \otimes_Y G_{22}^{ns} + J_\Omega \otimes_X \otimes_Y G_{22}^{s}] \tag{10.18a}$$

and its FFT-counterpart is

$$\mathbf{J}_\Omega = \mathbf{J}_0 + \mathbf{X}_\Omega FFT^{-1}\Big[\Big\{\overline{FFT_X\left(\overline{FFT_Y \mathbf{J}_\Omega}\right)} \times FFT_{XY}\mathbf{H}_{22}^{ns}\Big\} + \{FFT_{XY}\mathbf{J}_\Omega \times FFT_{XY}\mathbf{H}_{22}^{s}\}\Big] \tag{10.18b}$$

with bold-typed $M*M$ arrays $\mathbf{J}_0$, $\mathbf{J}_\Omega$, $\mathbf{X}_\Omega$, $\mathbf{H}_{22}^{s}$ and $\mathbf{H}_{22}^{ns}$, where FFT_U means that we apply on the two-dimensional array under consideration a direct Fast Fourier Transform with respect to dimension(s) $U(\equiv X$ and/or $Y)$ and where FFT^{-1} means that we perform the inverse FFT with respect to the two corresponding directions in the spectral domain.

The N^2 samples of functions J_0, J_Ω or χ_Ω (null outside D_Ω) yield $M*M$-arrays after extension to zero. The $\mathbf{H}_{22}^{s}$ and $\mathbf{H}_{22}^{ns}$ $M*M$-arrays are deduced from the discrete homologues $H_{22}^{s}(X_p, Y_q)$ and $H_{22}^{ns}(X_p, Y_q)$ [calculated like $H_{22}^{s}(X_m - X_p, Y_n - Y_q)$ and $H_{22}^{ns}(X_m + X_p, Y_n - Y_q)$] of the singular and regular parts of the Green's function (which is defined for any position of the source and observation points inside the domain D_Ω) as follows:

$$\mathbf{H}_{22}^{i} = \begin{cases} H_{22}^{i}(X_p, Y_q) & \text{if } \begin{cases} -N\Delta < X_p < +N\Delta \\ -N\Delta < Y_q < +N\Delta \end{cases} \\ 0 & \text{elsewhere} \end{cases} \tag{10.19}$$

where the superscript i is either s or ns, and where $H_{22}(X_p, Y_q)$ is given by (10.12a) when $i = ns$, and by (10.12b) when $i = s$.

Once the above relations are established, the solution methods are easily derived. First, let us consider the Neumann's series procedure. In that case, the basic functional relationship that relates the nth. iterate J_Ω^n to the $(n-1)$th. J_Ω^{n-1} is, starting from $n = 1$,

$$J_\Omega^n = J_0 + \chi_\Omega [J_\Omega^{n-1} ©_X \otimes_Y G_{22}^{ns} + J_\Omega^{n-1} \otimes_X \otimes_Y G_{22}^{s}] \qquad (10.20a)$$

and its FFT-counterpart is

$$\begin{aligned} \mathbf{J}_\Omega^n = &\mathbf{J}_0 + \mathbf{X}_\Omega FFT^{-1} \left[\left\{ \overline{FFT_X(\overline{FFT_Y \mathbf{J}_\Omega^{n-1}})} \times FFT_{XY} \mathbf{H}_{22}^{ns} \right\} \right. \\ &\left. + \left\{ FFT_{XY} \mathbf{J}_\Omega^{n-1} \times FFT_{XY} \mathbf{H}_{22}^{s} \right\} \right] \end{aligned} \qquad (10.20b)$$

Aitken's extrapolation allows us to speed up the rate of convergence (this should not necessarily be true every time and theoretically requires that the convergence be at least linear, but we have observed that phenomenon in all computations we made using Neumann's series). In effect, it is sufficient each three iterations (starting at $n = 2$) to replace the normal iterate J_Ω^n by a new one J'^n_Ω given by

$$J'^n_\Omega = J_\Omega^n - \frac{[J_\Omega^n - J_\Omega^{n-1}]^2}{J_\Omega^n - 2J_\Omega^{n-1} + J_\Omega^{n-2}} \qquad (10.20c)$$

Then we identify J'^n_Ω and J_Ω^n, continue the Neumann's expansion the next two steps, carry out again Aitken's extrapolation, and so on. Doing so has obviously a trade-off since we are (at least) obliged to store three $N * N$ arrays (non-null values of the currents at steps n, $n-1$ and $n-2$). The procedure is stopped when the iterates stay almost constant between two iterations (of the Neuman's kind), i.e., when the mean-squared norm $|(J_\Omega^n - J_\Omega^{n-1})/J_\Omega^0|^2$ becomes less than a small positive factor ε.

Second, let us consider the conjugate-gradient procedures. Whatever be the particular variant we use, we always have to define the direct operator, denoted A as in the above, and the adjoint operator, denoted A^*. We keep the same notations as previously. When acting onto functions E and F of (X,Y) which are null like χ outside the

domain D_Ω (we henceforth drop the Ω-dependence in order to avoid too many subscripts in the expressions), they are written as

$$AE = E - \chi[E \copyright_X \otimes_Y G_{22}^{ns} + E \otimes_X \otimes_Y G_{22}^{s}]$$

$$A^*F = F - \overline{[(\chi\overline{F}) \copyright_X \otimes_Y G_{22}^{ns} + (\chi\overline{F}) \otimes_X \otimes_Y G_{22}^{s}]} \qquad (10.21a)$$

and their FFT-counterparts are

$$\mathbf{AE} = \mathbf{E} - \mathbf{X} \times FFT^{-1}\left[\left\{\overline{FFT_X(\overline{FFT_Y\mathbf{E}})} \times FFT_{XY}\mathbf{H}_{22}^{ns}\right\} + \left\{FFT_{XY}\mathbf{E} \times FFT_{XY}\mathbf{H}_{22}^{s}\right\}\right]$$

$$\mathbf{A^*F} = \mathbf{F} - \overline{FFT^{-1}\left[\left\{\overline{FFT_X(\overline{FFT_Y(\mathbf{X} \times \bar{\mathbf{F}})})} \times FFT_{XY}\mathbf{H}_{22}^{ns}\right\} + \overline{\left\{FFT_{XY}(\mathbf{X} \times \bar{\mathbf{F}}) \times FT_{XY}\mathbf{H}_{22}^{s}\right\}}\right]} \qquad (10.21b)$$

The iterative procedures are schematized in Fig. 10.2, with choices of real-valued factors α_i and β_i depending on the type of procedure chosen; the objective function to be minimized is either the mean-square norm of the solution error $(J - J_{ex})$, letting J_{ex} be the solution we are looking for, which corresponds to the left-sided branchs of the trees, or of the residual $J_0 - AJ_{ex}$, which corresponds to the right-sided branchs. However, in both cases the minimization is stopped when the normalized mean-square norm of the residual is decreased enough, i.e., is lower than ε. The stopping criterion is similar to the one used in Neumann's expansion, since the latter is stopped when $J^n - J^{n-1}$ becomes small and is such that identity $J^n - J^{n-1} = J_0 - AJ^{n-1}$ applies. Note that the residual may not decrease during most iterations when using the solution error procedure. Note also that we replaced the usual $R^{n+1} = R^n - \alpha^n AP^n$ operation by $R^{n+1} = J_0 - AJ^{n+1}$ for it may avoid transfer of some numerical errors from the nth residual to the next one, and that normalized variants of these procedures could be employed.

Finally, it is interesting to count (approximately) the number of operations involved when using FFT's or not (note that the anomalous

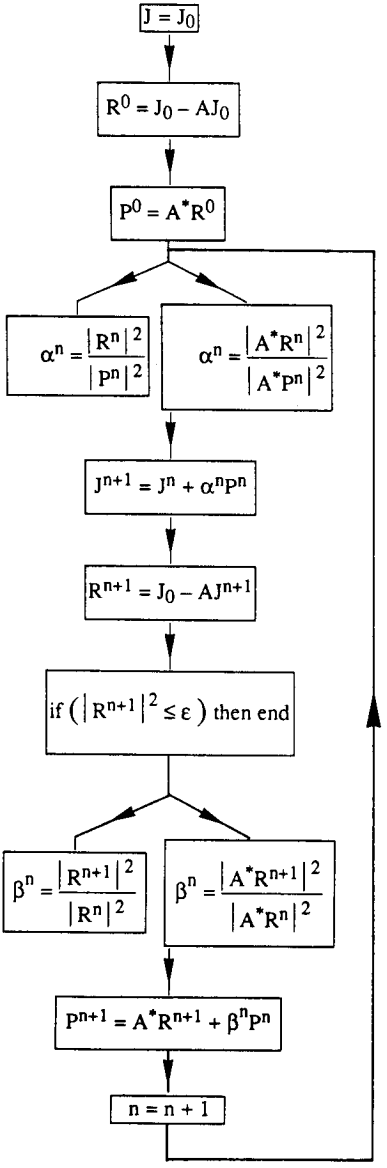

Figure 10.2 Usual conjugate-gradient schemes. Left branch: minimization of solution error, right branch: minimization of residuals. A is the direct operator, A^* is the adjoint one, $||^2$ denotes the mean square norm, J^n, P^n and R^n are respectively the unknown source, the conjugate direction and the residual at iteration n, with initial values J^0 (given by the user), P^0 and R^0; the procedure is stopped when the norm of the residual is small enough.

field is computed in both cases by direct summation, see (10.15a)). In the case of the Neumann's procedure, if we consider that each 1-D FFT requires $M \log M$ operations, we arrive at about $5M^2 \log M (+3M^2)$ operations per iteration, say, about $20N^2\ log 2N$ in the usual $M = 2N$ situation, compared to about N^4 operations per iteration when FFT's are not utilized. When using conjugate-gradient algorithms, these figures are multiplied by two. Consequently, even for small values of N (say $N \geq 10$), the number of operations is greatly reduced when using FFT's. On the contrary, preliminary computations and storage requirements get significantly heavier, about four times when using FFT's. Indeed, at the beginning, we have to calculate the elements of the $\mathbf{H}_{22}$ arrays and the FFT's of these arrays of order M; as the integrals over α are evaluated with the aid of a FFT algorithm of order $2N_\alpha$, we then have to carry out about $(2N)^2(2N_\alpha) \log 2N_\alpha + 2M^2 \log M$ operations, compared to about $N^2(2N_\alpha) \log 2N_\alpha$ without FFT's, while storage increases in proportion to $(M/N)^2$.

10.3 Numerical Results

10.3.1 Typical scattering cases

We illustrate the behavior of the iterative solution procedures in a few canonical configurations. Many other configurations could be studied, but we believe that those are various enough to show interest and limitations of these procedures. Similar configurations have also already been considered for the purpose of acoustical imaging studies we would like refer the reader to [1]. All the numerical results have been obtained by means of a standard UNIVAC 1190 sequential computer with single-precision world length, the so-called virtual mode of operation has been used in order to have enough space to store some of the arrays required.

As therein, we first introduce three typical models (see Fig. 10.3a) denoted by acronyms $Z1$, $Z2$ and $Z3$, and corresponding respectively to a low-contrast case (wave-velocities $c_2 = 1560$ m/s, $c_\Omega = 1540$ m/s), a medium-contrast case ($c_2 = 1800$ m/s, $c_\Omega = 1540$ m/s) and a high-contrast case ($c_2 = 1800$ m/s, $c_\Omega = 5900$ m/s). The upper half-space is water ($c_1 = 1470$ m/s), and the operating frequency is 2 MHz. For example, in case $Z2$ and $Z3$, the lower half-space could be some not firmly packed sand and in case $Z3$ the sound speed in the target is

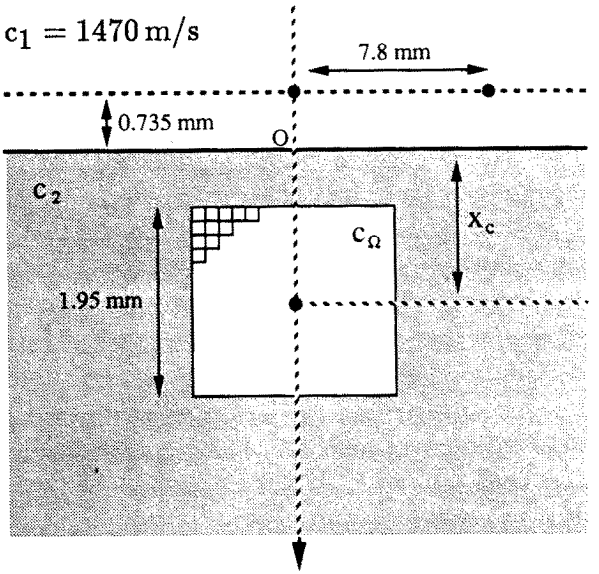

Figure 10.3a Configurations under investigation: square target.

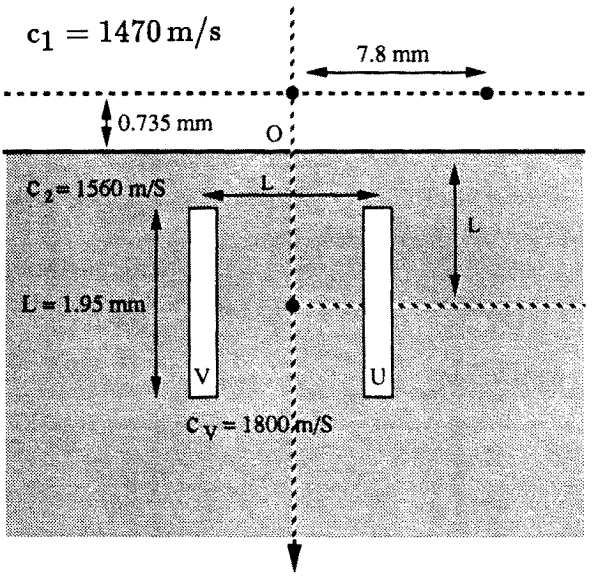

Figure 10.3b Configurations under investigation: two thin rectangles.

approximately that of compressional waves in steel. Wavelength λ_1 is 0.735 mm, wavelength λ_2 is either 0.74 mm ($Z1$) or 0.9 mm ($Z2$ or $Z3$). The target in the examples presented here is a homogeneous squared cylinder with side equal to 1.95 mm (i.e., $13\lambda_2/6$ in case $Z2$ or $Z3$), centered close to or far from the interface at depth $x_C = 1.8$ mm or 9.0 mm (2 and $10\lambda_2$ in both $Z2$ and $Z3$) and divided into $N^2 = 225$ cells with $\Delta = 0.13$ mm (i.e., $\approx \lambda_2/7$ in case $Z2$ or $Z3$). Sources and receivers are placed on the same line parallel to the interface at fixed distance $|x_R| = |x_S| = 0.735$ mm$=\lambda_1$; we compute the anomalous field every Δ between $y = -18$ and $+18$ mm ($\pm 20\lambda_2$ in $Z2$ or $Z3$) for a line source either central (at $y = 0$) or off-axis (at $y = 7.8$ mm$=60\Delta$).

In addition (see Fig. 10.3b), at the same 2 MHz frequency and in a low-speed medium D_2 ($c_2 = 1560$ m/s), we consider two homogeneous thin rectangles U and V, which have same geometry (length $L = 1.95$ mm, width $L/13$) and respective sound speeds c_U (with values 2500 or 5900 m/s) and $c_V = 1800$ m/s, and which are buried symmetrically with respect to the y -axis at depth $x_C = L$ and at distance L from one another. Each cylinder is divided into 13 squares ($\Delta = 0.15$ mm), and the target then consists of 169 cells whose only 26 have a contrast χ different from zero. The line source is placed at $y = 0$ or 7.8 mm at $\lambda_1 = 0.735$ mm above the interface. The anomalous fields are computed on the same line each Δ from -18 to $+18$ mm.

Results shown in Figs. 10.4 and 10.5 are variations of $\log(ERR)$ versus the number n of iterations, where ERR is the ratio of the residual mean-square norm $|R^n|^2$ to its initial value $|R^0|^2$, which we observe in the case of the square target (cases $Z1$, $Z2$ and $Z3$) when we expand the induced sources into Neumann's series (case $Z1$ only, as it does not converge in other cases) or when we use both variants of conjugate-gradient algorithm. In Fig. 10.4, these variations are given in each contrast case for the shallow target ($x_C = 1.8$ mm), the line source being either the central one (Fig. 10.4a) or the off-axis one (Fig. 10.4b); in addition, Fig.10.4c shows an "enlargement" of Fig. 10.4a in case $Z1$ only, which shows results obtained by Neumann's procedure and by conjugate-gradients. In Fig. 10.5, variations of the residual observed when using the conjugate-gradient algorithm that minimizes residuals are given in cases $Z1$ and $Z2$ for both square targets (shallow and deep) and both sources (on- and off-axis). Similar variations observed with the two-rectangle target are shown in Fig. 10.6 ($c_U = 2500$ m/s in Fig. 10.6a and $= 5900$ m/s in Fig. 10.6b). Amplitudes of the

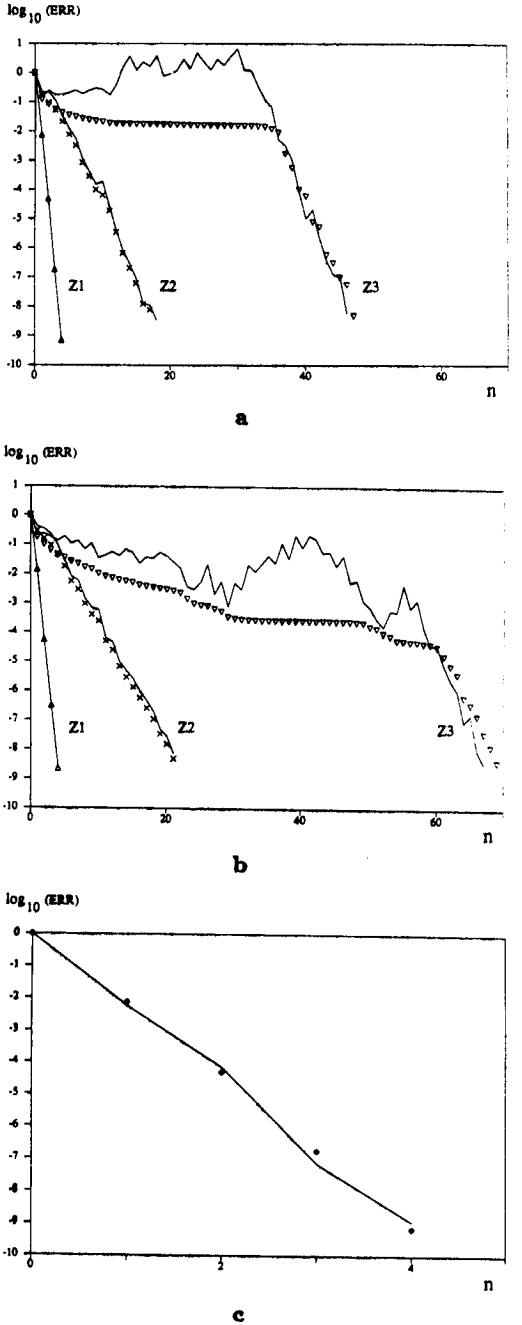

Figure 10.4 Normalized residual $ERR = |R^n|^2/|R^0|^2$ (log scale) versus number of iterations n for shallow square target in cases $Z1$, $Z2$ and $Z3$ when using conjugate-gradients (*lines*: minimisation of solution error, *symbols*: minimisation of residuals) for both sources (central: Fig. 10.4a, off-axis: Fig. 10.4b). In addition, Fig. 10.4c shows residuals in case $Z1$ with extrapolated Neumann's expansion (*line*) and both variants of conjugate-gradients (superimposed *symbols*).

anomalous fields p_A calculated in several of the above configurations with FFT's (drawn with full lines) or without FFT's (drawn with symbols) are shown in Figs. 10.7 to 10.11; we employ a logarithmic scale in most of these figures as discrepancies between these results are mostly apparent only for small relative amplitudes.

10.3.2 Conclusions

Results depicted in the figures have all been obtained using FFT's with $2N_\alpha = 2048$ points to calculate the various Fourier integrals. Increasing this number of points by a factor of two ($2N\alpha = 4096$) roughly doubles the computation time of these integrals but results remain almost the same (and are graphically identical). Also, since targets under investigation consist of at most $N * N = 15 * 15$ cells, arrays extended to $M * M = 32 * 32$ have been defined and Fourier transformed. These results and others (not shown) allow us to underline the following observations.

1) When discrete convolution and correlation products are not calculated by means of FFT's, CPU time depends upon (i) : the total number of cells N^2, which determines the number of samples of Green's functions we have to calculate beforehand and consequently the volume of preliminary computations, (ii) : the number of cells with contrast different from zero (the number of unknown, non-zero induced sources), which determines the number of operations within the diverse summations at each iteration. When these convolution/correlation products are calculated using FFT's, CPU time mostly depends upon rank M of the arrays; if the target consists of, e.g., two or more separated parts, we still have to manipulate arrays whose rank is proportional with length of the rectangle containing them and the computational burden remains of the same order of magnitude. But comparing performances of both types of procedures (with/without FFT's) is hindered by the fact (mentioned in the previous section) that we were forced to take a certain number of arrays as "virtual" ones, and a different number of them for each type, which significantly influences computation times. However, we can emphasize that

(i) : for "full" targets (like the square one), with $N = 15$ and $M/N \approx 2$, each iteration takes about twice as long without FFT's as with FFT's, whatever the iterative algorithm,

(ii) : for larger targets, the advantage of FFT-based procedures further increases (at $N = 23$, we observed a ratio of almost 5 in favor

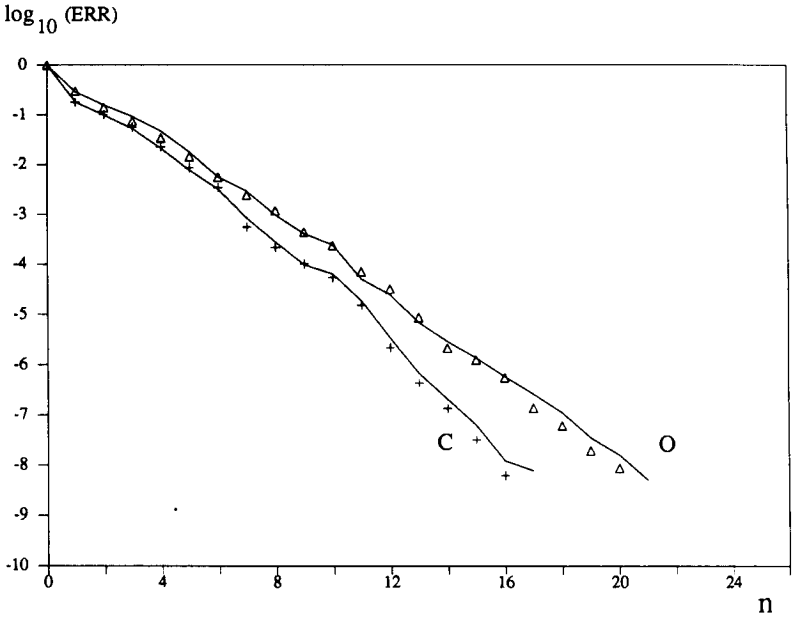

a

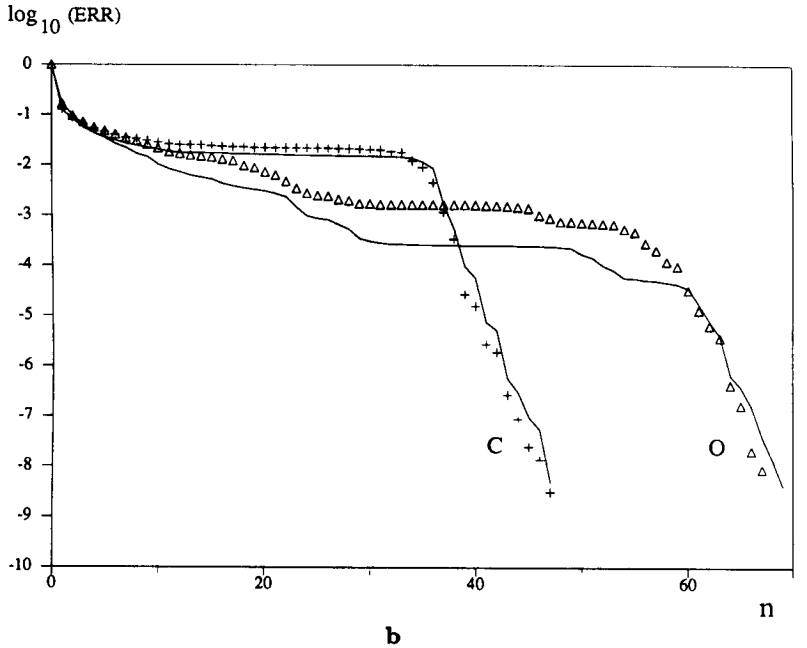

b

Figure 10.5 Normalized residual $ERR = |R^n|^2/|R^0|^2$ (log scale) versus number of iterations n for square target in cases $Z2$ (Fig. 10.5a) and $Z3$ (Fig. 10.5b) showing influence of target's depth (*lines*: shallow target, *symbols*: deep target) and of position of the source (central: lettering C, off-axis: lettering O). Conjugate-gradient algorithm with minimization of the residuals is applied.

of such procedures).

(iii) : on the contrary, for a hollow target, direct computations are faster than FFT-based ones, e.g., in the case of thin rectangles, directly carrying out each iteration is about five times faster, and storage is reduced accordingly.

2) Performances of conjugate-gradient solution methods are those expected. Both variants: minimizing residuals or minimizing solution error, yield stable induced sources J_Ω within about the same number of iterations and stable anomalous fields in less iterations (due to integration). Their numerical behaviors are different : residuals (as enforced) continuously decrease with the first one, and they may not with the other; then, variations of ERR become similar only after a certain number of iterations. Obviously, performances are functions of contrast (between target and half-spaces and between half-spaces) and of position of the line source, as is shown in Figs. 10.4 and 10.5 (square target).

(i) : The higher the contrast, the slower the rate of convergence. If contrast is important enough (e.g., $Z3$), we observe a long phase of "stagnation", where ERR either decreases extremely slowly (when minimizing residuals), or goes up and down in seemingly chaotic fashion (when minimizing solution error); with lower contrast (e.g., $Z1$ and at a lesser extent $Z2$), ERR decreases regularly — $\log(ERR)$ varies linearly vs. n — and almost identically using either variant.*

(ii) : At given contrast, the larger is the lateral distance between the position of the source and the target, the more difficult is the convergence, with the more influence for high contrast.

(iii) : Convergence is almost the same whether the target is buried close to the interface or buried far from it, all other parameters being kept fixed.

When dealing with the thin rectangles, that is, a partitioned target whose parts are of high-contrast with respect to one another and to the embedding, but remain of small size, it is like dealing with the low-contrast case $Z1$, since ERR decreases identically and at a fast pace

* We refer the reader to an investigation of radiation by thin-wire structures [7] which evidences (see Fig. 10.4) similar "stagnation" of residuals with Le Foll's and conventional algorithms (minimizing solution error and residuals, respectively). Reviewer A. G. Tijhuis suggests that it may be caused by an incorrect problem formulation, and the discussion is open.

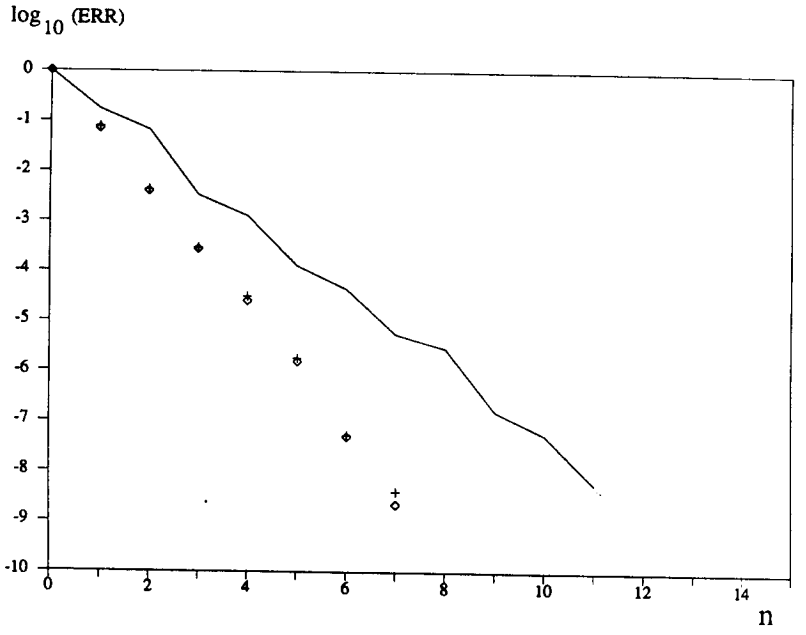

a

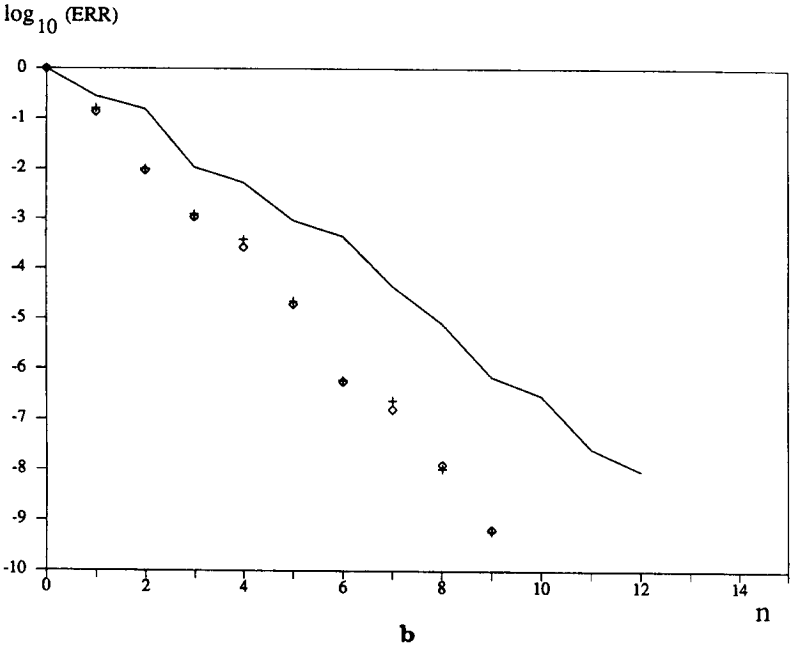

b

Figure 10.6 Normalized residual $ERR = |R^n|^2/|R^0|^2$ (log scale) versus number of iterations n for thin rectangles of medium-contrast (Fig. 10.6a: $c_U = 2500$ m/s) or of high-contrast (Fig. 10.6b: $c_U = 5900$ m/s) illuminated by central source, using extrapolated Neumann's expansion (*lines*) and conjugate-gradients (*symbols* + : minimization of solution error, ◇ : minimization of residuals).

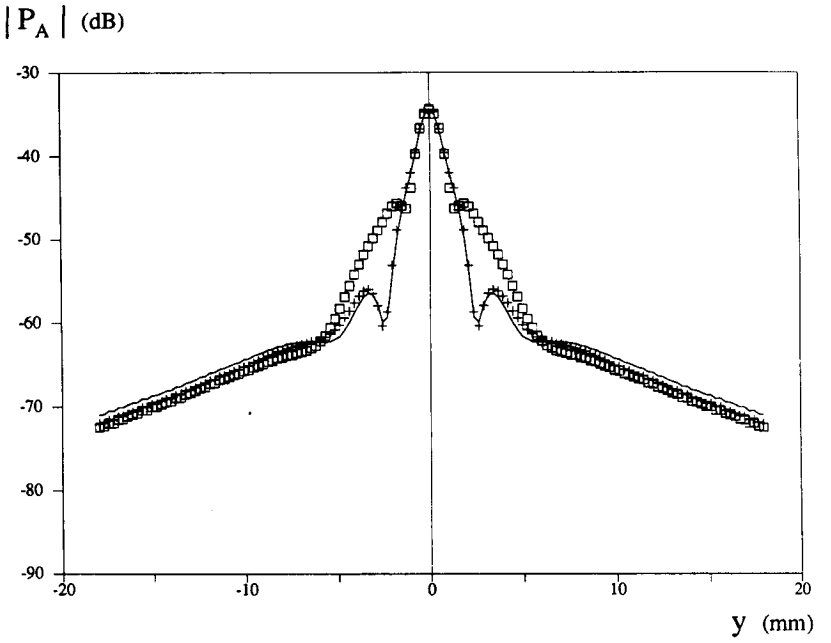

Figure 10.7 Anomalous field p_A (in dB) on the probing line for shallow square target in case $Z2$ (central source only) as a function of stopping criterion (ERR is compared to ε). *Symbol* : Born's approximated field (the field within the target is equated to the incident field, e.g., $n = 0$); *symbol* + : $\varepsilon = 10^{-2}$; *line* : $\varepsilon = 10^{-4}$. (At lower ε anomalous fields become graphically identical with those for $\varepsilon = 10^{-4}$).

with both conjugate-gradients, whereas at most one or two additional iterations are needed when the source is placed (transversely) far away from the target.

3) Extrapolated Neumann's expansion is confirmed to be quite efficient for low-contrast and/or small scatterers, like the thin rectangles (see Fig. 10.6) or like the square target in case $Z1$ (see Fig. 10.4c); the convergence rate is the same as or slightly slower than with conjugate-gradients and computation time per iteration is approximately twice shorter, with smaller storage. Convergence depends as usual on the scattering configuration investigated; for example (not shown), with the square target in case $Z2$, the expansion does not converge, ERR strongly increasing after the first few iterations, and this already hap-

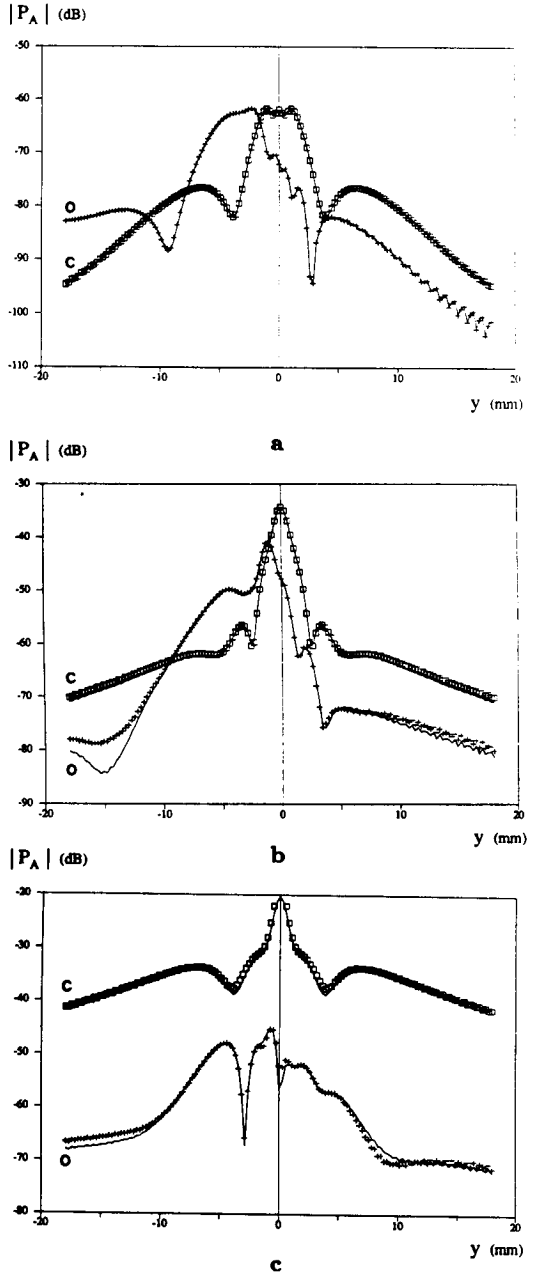

Figure 10.8 Anomalous field p_A (in dB) on the probing line for shallow square target, in cases $Z1$ (Fig. 10.8a), $Z2$ (Fig. 10.8b) and $Z3$ (Fig. 10.8c) and for both sources (central: lettering C, off-axis: lettering O), calculated by using conjugate-gradients ($\varepsilon = 10^{-8}$) with FFT's (*lines*) or without (*symbols*). (Anomalous fields for small enough ε do not depend upon the type of minimization — solution error or residuals.)

pens at the second one in case $Z3$.

4) Convergence of anomalous fields is, as noted in the above, faster than convergence of sources induced within the target (compare Fig. 10.7 that shows typical evolution of the anomalous fields versus number of iterations and Fig. 10.5a that shows corresponding evolution of the residuals associated to the induced sources). This results from summing up fields radiated by every target's cell to calculate the anomalous field. Attaining ERR values of the order of 10^{-4} then yields suitably accurate fields in low- and median-contrast cases (actually, when ERR decreases regularly), but this limit is generally not low enough in high-contrast cases (e.g., $Z3$) where we have to proceed further in order to leave the stagnation phase ($ERR \approx 10^{-6}$ appears suitable). However, such observations may be too problem-dependent to be adequate to other scattering or radiation problems.

5) Anomalous fields computed both ways (with/without FFT's) are in very good agreement, save exception.

(i) : Identical results are obtained in low-contrast case $Z1$ for any positions of target, sources and receivers.

(ii) : In median-contrast case $Z2$, we may observe some discrepancy, but when that happens, it only does for very low field amplitudes (about 30 dB or more below field maxima) and at large transverse distance $|y|$; this discrepancy is more visible for the off-axis source than for the central one. However, using absolute scales (see Fig. 10.9) puts this phenomenon in right proportion, and confirms that we get at least the same three first significant digits with and without FFT's. (There is no physical meaning to the small oscillations with period of one or two Δ that often occur when the above discrepancy is observed.) Similar observations are made with the hollow target, even in case of high-contrast.

(iii) : In high-contrast case $Z3$, the fact that numerical results slightly differ from one another for low level/far off-axis fields generally becomes more noticeable (and in that case some oscillations of stronger amplitude than with lower contrasts appear), or it may also not be observed at all (shallow target with on-axis source). More surprising is the discrepancy between anomalous fields on the $\underline{y}$-axis or very close to it (up to about 4Δ) that occurs for the shallow target illuminated by the central source (Fig. 10.9c). This might be related to the computations of the correlation products. Indeed, it is clear that : the stronger the contrast between half-spaces (D_1, D_2), the more important the contri-

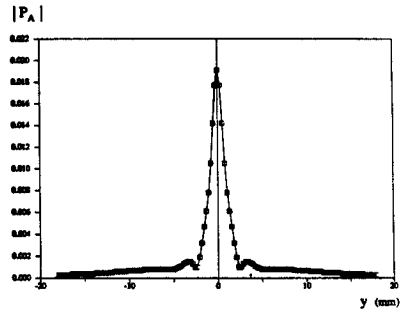

a

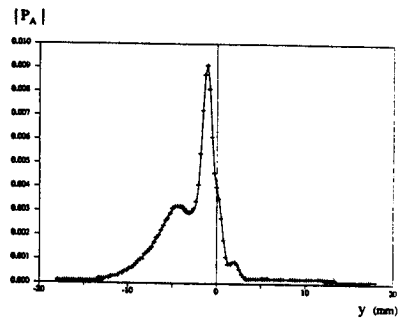

b

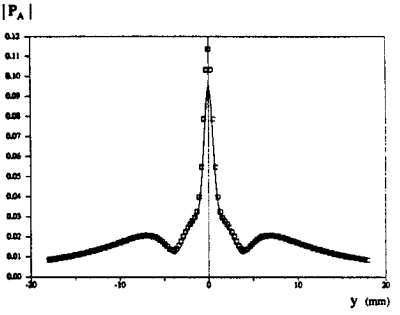

c

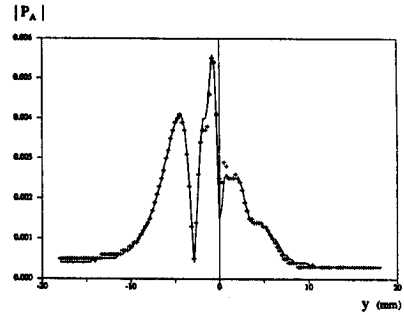

d

Figure 10.9 Examples of Fig. 10.8b and Fig. 10.8c: shallow square target, cases $Z2$ and $Z3$, with FFT's (*lines*) or without (*symbols*), depicted using absolute scale for p_A. Case $Z2$: Fig. 10.9a and Fig. 10.9b, case $Z3$: Fig. 10.9c and 10.9d, central source : Fig. 10.9a and 10.9c, off-axis source: Fig. 10.9b and 10.9d.

bution of such products to sources within the target (when $D_1 \approx D_2$, contributive terms are mostly the convolution products, which are accurately calculated by FFT's), and that : the stronger the contrast of the target with respect to D_2, the more important is/may be the consequence of small discrepancies when computing these sources. However, considering the first point alone is not enough, for results do agree in case $Z2$ but differ in case $Z3$ with the same stratified embedding in both cases, and at the time of writing, this leaves the door open to some speculation. This particular problem aside, agreement between results computed with or without FFT's agree (in short, we may count on identical two — often three — first significant digits).

Finally, we would like to mention that two problems of interest lie ahead. First, the above analysis has been carried out with using a simple implementation of the method of moments; it is not sure that the piecewise-constant expansion functions we utilized are sufficient for every kind of buried target, whose shape and contrast may be such that the induced sources vary too fast to be modeled with good accuracy with our choice of functions. However, it would be interesting to know if the gain in accuracy on the anomalous field we might observe with better suited functions is worth the increase in complexity of the calculations. Second, in practical applications in non-destructive testing, the role of variations in density (in ultrasonics) and of permeability (in electromagnetics) may be important and it is necessary to define a fast computational tool that can take them into account; in particular, when density or permeability of the half-spaces D_1 and D_2 differ, the new Green's function has the same shape than the one used herein, and the calculations can be performed the same way, but when, in addition, the target consists of parts with different density or permeability, contour integrals must be estimated.

Acknowledgment

We gratefully acknowledge A. G. Tijhuis for his careful reading and his constructive criticism, which in particular helped us to make the necessary modifications to the Fourier processing.

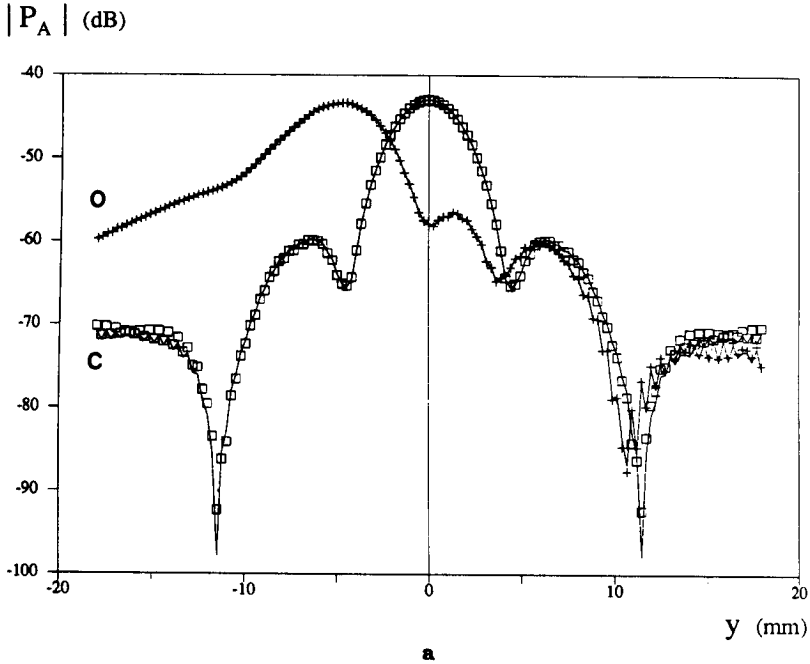

a

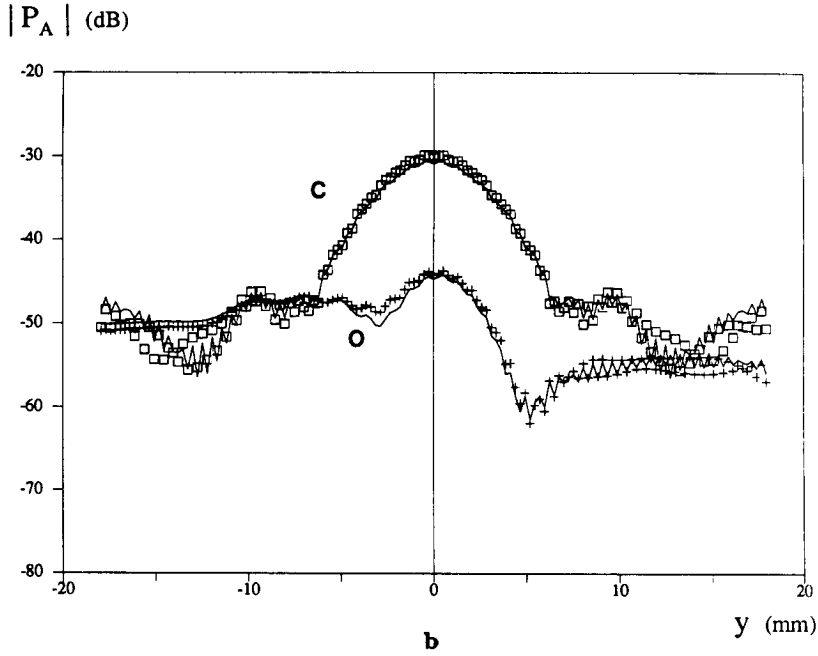

b

Figure 10.10 Anomalous field p_A (in dB) on the probing line for deep square target, in cases $Z2$ (Fig. 10.10a) and $Z3$ (Fig. 10.10b) and for both sources (central: lettering C, off-axis: lettering O), calculated by using conjugate-gradients ($\varepsilon = 10^{-8}$) with FFT's (*lines*) or without (*symbols*).

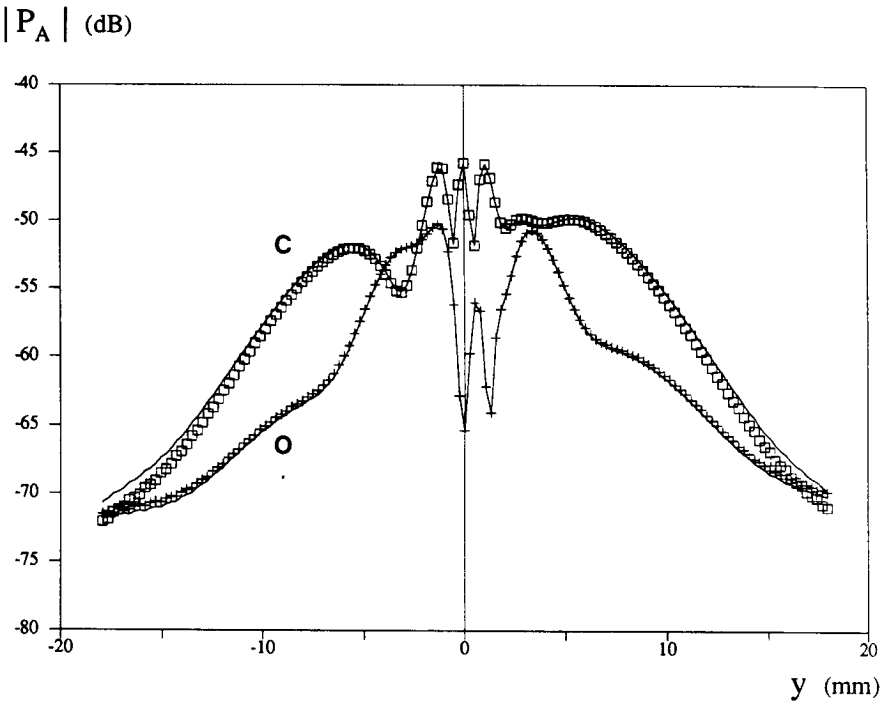

Figure 10.11 Anomalous field p_A (in dB) on the probing line for two thin rectangles of high-contrast ($c_U = 5900$ m/s) and for both sources (central: lettering C, off-axis: lettering O), calculated by using conjugate-gradient ($\varepsilon = 10^{-8}$) with FFT's (*lines*) or without (*symbols*).

References

[1] Duchêne, B., D. Lesselier, and W. Tabbara, "Acoustical imaging of 2-D fluid targets buried in half-space: a diffraction tomography approach," *IEEE Trans. Ultrason. Ferroelec. Freq. Control*, **UFFC-34**, 5, 540–549, 1987.

[2] Duchêne, B., D. Lesselier, and W. Tabbara, "Acoustical imaging of 2-D fluid targets buried in half-space: a diffraction tomography approach using line sources insonification," *Electromagnetic and Acoustic Scattering Detection and Inverse Problems*, C. Bourrely *et al.* Eds., World Scientific Publ. Co., London, 1989.

[3] Osumi, N., and K. Ueno, "Microwave holographic imaging of underground objects," *IEEE Trans. Atennas Propagat.*, **AP-33**, **2**,

152–159, 1985.

[4] Chommeloux, L., Ch. Pichot, and J. Ch. Bolomey, "Electromagnetic modeling for microwave imaging of cylindrical buried inhomogeneities," *IEEE Trans. Microwave Theory Tech.*, **MTT-34**, **10**, 1064–1076, 1986.

[5] Michiguchi, Y. *et al.*, "Development of signal processing methods for imaging buried pipes," *IEEE Trans. Geosci. Remote Sens.*, **GE-25**, **1**, 11–15, 1987.

[6] Azimi, M., and K. C. Kak, "Distorsion in diffraction tomography caused by multiple scattering," *IEEE Trans. Med. Imaging*, **MI-2**, **4**, 176–195, 1983.

[7] Lesselier, D., D. Vuillet-Laurent, F. Jouvie, and W. Tabbara, "Iterative solution of some direct and inverse problems in electromagnetics and acoustics," *Electromagnetics*, **5**, 2–3, 147–189, 1985.

[8] Harrington, R. F., "The method of moments in electromagnetics," *J. Electromag. Waves Appl.*, **1**, 3, 181–200, 1987.

[9] Miller, E. K., "A selective survey of computational electromagnetics," *IEEE Trans. Antennas Propagat.*, **AP-36**, **9**, 1281–1305, 1988.

[10] Duchêne, B., and W. Tabbara, "Characterization of a buried cylindrical object from its scattered field," *IEEE Trans. Son. Ultrason.*, **SU-31**, **6**, 658–663, 1984.

[11] Izadian, J., L. Peters, and J. H. Richmond, "Computation of scattering from penetrable cylinders with improved numerical efficiency," *IEEE Trans. Geosci. Remote Sens.*, **GE-22**, **1**, 52–61, 1984.

[12] Datta, S. K., and N. El-Akily, "Diffraction of elastic waves by cylindrical cavity in a half-space," *J. Acoust. Soc. Am.*, **64**, **6**, 1692–1699, 1978.

[13] Karlsson, A., "Scattering from inhomogeneities in layered structures," *J. Acoust. Soc. Am.*, **71**, **5**, 1083–1092, 1982.

[14] Bennett, C. L., and H. Mieras, "Space-time integral equation solution for hard and soft targets in presence of a hard and soft half-space," *Wave Mot.*, **5**, 399–411, 1983.

[15] Niwa, Y., S. Hirose, and M. Kitahara, "Application of the bound-

ary integral equation (B.I.E.) method to transient response analysis of inclusions in a half-space," *Wave Mot.*, **8**, **1**, 77–91, 1986.

[16] Schuster, G. T., and L. C. Smith, "Modeling scatterers embedded in plane-layered media by an hybrid Haskell-Thomson and boundary integral equation method," *J. Acoust. Soc. Am.*, **78**, **4**, 1387–1394, 1985.

[17] Umashankar, K. R., "Numerical analysis of electromagnetic wave scattering and interaction based on frequency-domain integral equation and method of moments techniques," *Wave Mot.*, **10**, **6**, 493–525, 1988.

[18] Hestenes, M., and E. Stiefel, "Method of conjugate gradients for solving linear systems," *J. Res. Nat. Bur. Stand.*, **49**, **152**, 409–436, 1952.

[19] Ray, S. L., and A. F. Peterson, "Error and convergence in numerical implementations of the conjugate gradient method," *IEEE Trans. Antennas Propagat.*, **AP-36**, **12**, 1824–1827, 12, 1988.

[20] Tijhuis, A. G., *Electromagnetic Inverse Profiling. Theory and Numerical Implementation.* VNU Science Press, Utrecht, 1987.

[21] Roger, A., "Theoretical study and numerical resolution of inverse problems via the functional derivatives," in *Inverse Methods in Electromagnetic Imaging*, Boerner W. M. *et al.* Eds., Reidel Publ. Comp., Dordrecht, Part I, 111–120, 1985

[22] Daniel, J. W., "The conjugate-gradient method for linear and nonlinear operator equation," *SIAM J. Num. Anal.*, **4**, **1**, 10–26, 1967.

[23] Bolomey, J. Ch., and W. Tabbara, "Numerical aspects on coupling between complementary boundary value problems," *IEEE Trans. Antennas Propagat.*, **AP-21**, **3**, 356–363, 1973.

[24] Sarkar, T. K., K. R. Siarkiewicz, and R. F. Stratton, "Survey of numerical methods for solution of large system of linear equations for electromagnetic field problems," *IEEE Trans. Antennas Propagat.*, **AP-29**, **6**, 847–856, 1981.

[25] Herman, G. C., and P. M. van den Berg, "A least-square iterative technique for solving time-domain scattering problems," *J. Acoust. Soc. Am.*, **72**, **12**, 1947–1953, 1982.

[26] van den Berg, P. M., A. T. de Hoop, A. Segal, and N. Praagman,

"The computational model of the electromagnetic heating of biological tissue with application to hyperthermia cancer therapy," *IEEE Trans. Biomed. Eng.*, **BME-30**, **12**, 797–815, 1983.

[27] Dudley, D. G., "Error minimization and convergence in numerical methods," *Electromagnetics*, **5**, 2–3, 89–97, 1985.

[28] Sarkar, T. K., E. Arvas, and S. M. Rao, "Application of the Fast Fourier Transform and the conjugate gradient method for efficient solution of electromagnetic scattering from both electrically large and small conducting bodies," *Electromagnetics*, **5**, 2–3, 99–122, 1985.

[29] Mittra, R., and C. H. Chan, "Iterative approaches to the solution of electromagnetic boundary value problems," *Electromagnetics*, **5**, 2–3, 123–146, 1985.

[30] van den Berg, P. M., "Iterative schemes based on the minimization of the error in field problems," *Electromagnetics*, **5**, 2–3, 237–262, 1985.

[31] Peterson, A. F., and R. Mittra, "Method of conjugate gradient for the numerical solution of large-body electromagnetic scattering problem," *J. Opt. Soc. Am. A*, **2**, 6, 971–977, 1985.

[32] Borup, D. T., and O. P. Gandhi, "Fast-Fourier Transform method for calculation of SAR distributions in finely discretized inhomogeneous models of biological bodies," *IEEE Trans. Microwave Theory Tech.*, **32**, 4, 255–360, 1984.

[33] Sarkar, T. K., X. Yang, and E. Arvas, "A limited survey of various conjugate gradient methods for solving complex matrix equations arising in electromagnetic wave interactions," *Wave Mot.*, **10**, 6, 527–546, 1988.

[34] Sarkar, T. K., "On the application of the generalized biconjugate algorithm," *J. Electrom. Waves Appl.*, **1**, 3, 223–242, 1987.

[35] Peterson, A. F., and R. Mittra, "Convergence of the conjugate gradient method when applied to matrix equations representing electromagnetic scattering problems," *IEEE Trans. Antennas Propagat.*, **AP-34**, **12**, 1447–1454, 1986.

[36] Peterson, A. F., C. F. Smith, and R. Mittra, "Eigenvalues of the moment method matrix and their effect on the convergence of the conjugate gradient algorithm," *IEEE Trans. Antennas Propagat.*,

AP-36, 8, 1177–1179, 1988.

[37] Kas, A., and E. L. Yip, "Preconditioned conjugate gradient methods for solving electromagnetic problems," *IEEE Trans. Antennas Propagat.*, **AP-35**, 2, 147–152, 1987.

[38] Su, C-C., "Calculation of electromagnetic scattering from a dielectric cylinder using the conjugate gradient method and FFT," *IEEE Trans. Antennas Propagat.*, **AP-35**, 12, 1418–1425, 1987.

[39] Richmond, J. H., "Scattering by a dielectric cylinder of arbitrary cross-section shape," *IEEE Trans. Antennas Propagat.*, **AP-13**, 3, 334–341, 1965.

[40] Richmond, J. H., "TE-wave scattering by a dielectric cylinder of arbitrary cross-section shape," *IEEE Trans. Antennas Propagat.*, **AP-14**, 4, 460–464, 1966.

[41] Joachimovicz, N., and Ch. Pichot, "Comparison of three integral formulations for the 2D-TE scattering problem," *IEEE Trans. Microwave Theory Tech.*, **MTT-38**, 2, 178–185, 1990.

[42] Dahlquist, G., and A. Bjorck, translated by N. Anderson, *Numerical Methods*, Prentice Hall Inc., Englewood Cliffs, N.J., 1974.

[43] Brigham, E. O., *The Fast Fourier Transform*, Prentice Hall Inc., Englewood Cliffs, N.J., 1974.

Erratum

Numerical results observed in one of the test cases (the high contrast case $Z3$) are partly suffering from a programming error. Adequate correction leads to magnitudes of the fields calculated without FFT shown in Figs. 10.9c and 10.9d which are almost the same as those calculated with FFT (that is, the agreement between both types of results is the same as in the other test cases). In these two figures, the curves drawn with symbols should almost overlap those drawn with full lines (which stay unchanged). Consequently, in part 2.2, the open problem discussed in the conclusive comment numbered "5 (iii)" is solved. The last sentence of the comment should simply read "Results computed with or without FFT's agree."